A&A 448, 367–374 (2006)
DOI: 10.1051/0004-6361:20054139


Astronomy & Astrophysics

# Radiative transfer in cylindrical threads with incident radiation

## III. Hydrogen spectrum

P. Gouttebroze

Institut d'Astrophysique Spatiale, Univ. Paris XI/CNRS, Bât. 121, 91405 Orsay Cedex, France
e-mail: goutte@ias.u-psud.fr

Received 1 September 2005 / Accepted 30 September 2005

**ABSTRACT**

A numerical code is proposed for the solution of NLTE radiative transfer equations in long cylinders, including multilevel atoms and anisotropic incident radiation (which implies a 2-dimension treatment of the radiation field). It is applied to the modelling of the hydrogen spectrum emitted by magnetic loops imbedded in the solar corona. The model hydrogen atom includes 10 levels and one continuum. The intensities emitted by loops in the most important hydrogen lines and in the Lyman continuum are discussed using a set of isothermal and isobaric models. The case of loops with a radial temperature gradient is also investigated.

**Key words.** methods: numerical – radiative transfer – line: profiles – line: formation – Sun: prominences – Sun: corona

## 1. Introduction

When observed at high angular resolution, the outer solar atmosphere appears to be constituted of many thread-like structures, or loops, whose extension and contrast vary with the wavelength of observation. This structuration is interpreted as being the consequence of the solar magnetic field, while the variations of brightness with wavelength likely result from variations mainly in temperature but also in pressure and velocity. High resolution H$\alpha$ spectroheliograms show the cooler parts of the loop system, while hotter parts appear in UV lines.

This paper is the third in a series dedicated to NLTE radiative transfer in cylindrical objects, with the aim of modelling these elongated structures embedded in the solar corona. Paper I (Gouttebroze 2004) was restricted to the 1D cylindrical problem, where both the medium properties and the radiation field are invariant by translation along the axis and rotation around it. This 1D case allows treatment of the long threads whose axis is vertical, so that they receive incident radiation independent of azimuth. This has been treated previously by many authors. In particular, Heaslet & Warming (1966) performed a very detailed analytical treatment of the problem. Leung (1976) and Heasley (1977) proposed numerical methods based on finite differences and variable Eddington factors, while Heasley applied the method to the case of a multilevel (Ca II) atom. In Paper I, we treated the same kind of problem by the multilevel accelerated $\Lambda$-iteration (MALI) technique and applied it to a 20-level plus continuum hydrogen atom with correction of electron density.

In Paper II (Gouttebroze 2005), we developed a 2D code allowing non-isotropic incident radiation. Here, it is useful to recall the existence of different problems under the same appellation "2D cylindrical problem". While there are three cylindrical coordinates (radius $r$, azimuth $\psi$, and distance-along-axis $z$), two of them are active in a 2D cylindrical problem, while the radiation field is invariant with respect to the third one.

The problem where $r$ and $z$ are the active variables is appropriate to some astrophysical objects, such as accretion disks or vertical cylinders of finite length, and it has been treated by several authors. For instance, the Monte-Carlo method was used by Avery et al. (1969) to compare the emissions of a finite-length cylinder with those of a slab. Avery & House (1969) used the same method to compute the emission of the Ca II K line by a spicule with vertical axis. The method was generalized by Avery (1970) to introduce velocity fields. Magnan (1970, 1972) also used the Monte-Carlo method to treat this 2D $(r, z)$ cylindrical problem. All these Monte-Carlo studies assumed a two-level atom. More recently, Van Noort et al. (2002) proposed a method to treat different 2D problems: cartesian, spherical, and cylindrical $(r, z)$ with a common short-characteristics scheme.

In Paper II, the structures under study (solar loops) had a small radius-to-length ratio, so that longitudinal transfer effects could be neglected, and the active variables are $r$ and $\psi$. The third possibility, where $z$ and $\psi$ would be the active variables, does not seem to be physically relevant. The $(r,\psi)$ case was already treated by Gouttebroze et al. (1986) using a Monte-Carlo

method, but with very restrictive conditions (homogeneous medium, 2-level atom, moderate optical depths).

In this paper, we combine the multilevel formulation of Paper I with the 2D transfer method of Paper II to build a new code and apply it to the computation of the hydrogen spectrum emitted by solar loops.

## 2. Computational methods

The numerical code developed to solve the present problem is a synthesis of two previous ones:

- the 1D hydrogen code presented in Paper I for what concerns the treatment of statistical equilibrium and the sequence of computations;
- the 2D 2-level code of Paper II, concerning the determination of incident intensities and the radiative transfer routines.

Since all useful equations have already been given in either Paper I or Paper II, it does not seem necessary to reproduce them here.

### 2.1. Incident intensities

The computation begins by determining incident intensities at the surface of the cylinder. As described in Paper II, the process consists of determining the intensities coming from a sphere of a given radius, located at a given distance in a given direction with respect to the cylinder. The resulting intensities are stored in a large array depending on five parameters:

- the azimuthal position $\psi$ around the cylinder;
- two direction angles: $\theta$ and $\zeta$. A former $100 \times 100$ array is subsequently reduced to $4 \times 4$ one, as described in Paper II;
- the atomic transition number;
- the frequency within each atomic transition.

### 2.2. Radiative transfer and statistical equilibrium

For the chemical composition of the gas inside the cylinder, we assume a mixture of hydrogen and helium, in the proportion of 1 atom of helium for 10 atoms of hydrogen. Helium is assumed to be neutral, so that the electron density is determined only by the hydrogen ionization. The model cylinder is then defined by its external radius $R$ and three physical parameters: temperature $T$, gas pressure $P$, and microturbulent velocity $\xi$, which are fixed a priori. These three parameters are functions of the distance to the axis $r$ and of the azimuth $\psi$. However, they are usually taken as constant, unless there is a reason to do otherwise (for instance, $T$ varies with $r$ in Sect. 4). On the contrary, the electron density $N_e$ is a result of computation and does vary with $r$ and $\psi$.

The initial values of hydrogen level populations $N_j$ and of electron density are determined as follows:

- we assume that the structure is optically thin in every transition and determine the mean intensity by averaging the incident intensities coming from all directions;
- we start from $N_e = 0.5 N_H$ (where $N_H$ is the total hydrogen density);
- we compute the collisional and radiative transition probabilities for all atomic transitions and solve the statistical equilibrium equation to obtain the populations $N_j$. This yields a new value for $N_e$;
- we iterate on $N_j$ and $N_e$ until the convergence of all populations.

At this stage, we have a homogeneous model with constant populations $N_j$ and $N_e$ inside the cylinder. Then, we begin the MALI process, alternatively solving the radiative transfer and the statistical equilibrium equations to determine the populations $N_j$ as functions of $r$ and $\psi$. The method for solving the preconditioned equations of statistical equilibrium, derived from Werner & Husfeld (1985), was described in Paper I. Different treatments of the radiative transfer equation are applied to the different transitions, according to their opacities. First, we evaluate the mean optical thickness $\tau$ along the radius for the frequency corresponding to the maximum of opacity: at line center for a discrete transition, at the head for a bound-free continuum. If the optical thickness is very small, say $\tau < 10^{-3}$, the intensities are taken as constant. For optically thick transitions, i.e. $\tau > 1$, the ALI method with preconditioning is used. For intermediate values, where there is no problem of slow convergence, pure $\Lambda$-iteration is applied. The preconditioning is obtained by subtracting the diagonal of the $\Lambda$ operator, as initially suggested by Olson et al. (1986). The procedure for computing the diagonal $\Lambda$ operator, inspired by Rybicki & Hummer (1991), is described in Paper II. Optionally, the method of Ng (1974) may be used to further accelerate the convergence of populations: every four iterations, the values of $N_j$ of the last iteration are combined with those of the three preceding iterations. The loop on level populations is included in another loop for the correction of electron density (generally, one iteration for $N_e$ corresponds to 4 or 8 iterations for $N_j$).

### 2.3. Construction of a semi-toric loop

Different model cylinders may be assembled together to produce a loop model. As an example, we consider here a semi-toric loop. The radius of the torus section is fixed (rather arbitrarily) to 1000 km, while the axis of the torus is a semi-circle of radius $10^4$ km. The method is schematized in Fig. 1: at different positions along the loop, we consider the tangent cylinder, and apply the 2D code to obtain the absorption coefficients $\kappa_\nu$ and the source functions $S_\nu$ as functions of $r$ and $\psi$ for the different transitions. The boundary conditions are given by the inclination angle $\alpha$ and the altitude $H$, which define the incident intensities. Once these computations are completed, it is possible to obtain $\kappa_\nu$ and $S_\nu$ by interpolation for any point inside the loop. Then, by integrating the basic transfer equation along the rays crossing the loop, we can obtain the intensities emitted in any direction. In the following, we consider only the intensities emitted perpendicular to the plane that contains the axis of the torus.

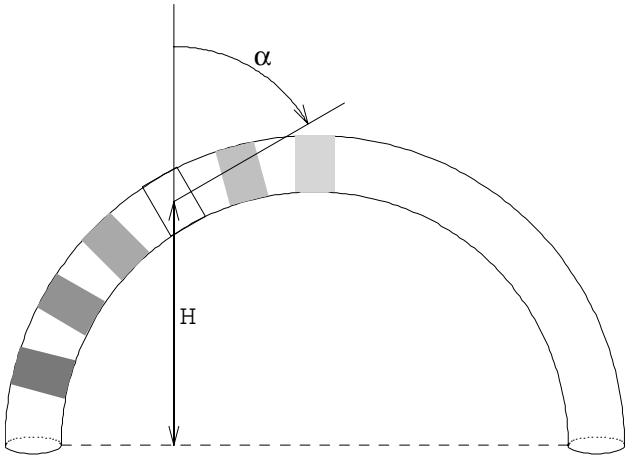


**Fig. 1.** Construction of a semi-toric loop.

## 3. Isobaric-isothermal loops

### 3.1. Models

The isobaric-isothermal loops are investigated with the help of 8 models, whose temperature and pressure are indicated in Table 1. Their geometric properties are those described in Sect. 2.3, while the microturbulent velocity is fixed to 5 km $s^{-1}$. These pressures correspond to values commonly allowed for the solar corona. The temperatures under investigation are relevant for the emission in hydrogen lines.

### 3.2. Results for Model 2

Model 2 is representative of cool loops that may be encountered in the modelling of prominence cores, for instance. We use it to illustrate the formation of hydrogen lines. Figure 2 represents the loop as it would be seen in the two first Lyman lines and the two first Balmer lines, with the intensities integrated over wavelength. In each case, the lower part of the loop is brighter than the upper one, due to the higher excitation of hydrogen atoms, which is itself the result of the greater irradiation by solar lines and continua. However, there is a difference in appearance between Lyman and Balmer lines, and even between L$\alpha$ and L$\beta$. If we observe the top of the loop and look at the variation in intensity between the internal and external edges (Fig. 3), it appears that the maximum of intensity for L$\beta$ is located very close to the internal edge. This is also true for other optically thick transitions, such as L$\gamma$ or the Lyman continuum (not represented here). On the contrary, for the optically thin Balmer lines, the maximum of intensity is shifted towards the middle of the loop, at a distance of about 1/4 of the diameter in the present case. The difference between L$\alpha$ and L$\beta$ comes from the particular profile of L$\alpha$. The line profiles of L$\alpha$, L$\beta$, and H$\alpha$ are displayed in Fig. 4 as functions of both wavelength and position across the upper part of the loop. For the model under investigation, L$\alpha$ is the only reversed line and it has large wings that contribute significantly to the emission. In contrast, L$\beta$ is a pure emission line with a narrow and abrupt profile, so that the main part of the emission comes from the optically thick core of the line. This contribution of the L$\alpha$ wings, which are optically thin, explains why the maximum of intensity is not located very close to the lower edge of the loop (as for L$\beta$) but shifted somewhat higher, in spite of the fact that the L$\alpha$ core is optically thicker than the L$\beta$ one.

**Table 1.** Properties of isobaric-isothermal models.

| Model number | Temperature (K) | Gas pressure (dyn $cm^{-2}$) |
|---|---|---|
| 1 | 7500 | 0.02 |
| 2 | 7500 | 0.1 |
| 3 | 7500 | 0.5 |
| 4 | 5000 | 0.1 |
| 5 | 10 000 | 0.1 |
| 6 | 15 000 | 0.1 |
| 7 | 20 000 | 0.1 |
| 8 | 30 000 | 0.1 |

### 3.3. Temperature effects

Keeping the gas pressure to 0.1 dyn $cm^{-2}$, we use six models to study the effects of temperature from 5000 to 30 000 K on emitted intensities. Temperature reduces the density of hydrogen atoms in the ground level by several means. First, the gas density itself is lowered through the equation of state, the pressure being constant. Second, temperature activates the processes of excitation and ionization, so that the ratios $N_j/N_1$ ($j > 1$) and $N_e/N_1$ rise. The global result is a rapid decrease in optical thicknesses in Lyman lines and continuum, as temperature increases. The behavior of higher levels is more complicated, because the equation of state and the ionization process tend to reduce the population of these levels, but the increase in excitation acts in the opposite direction. As a result, the populations of these levels first increase with temperature, reach a maximum, and finally decrease. The net effect of these changes of populations on frequency-integrated intensities is shown in Fig. 5. The maximum intensities measured for each image are plotted as functions of temperature for different transitions. The L$\alpha$ line intensity shows small variations under 10 000 K, then increases to reach a maximum around 20 000 K, and finally decreases towards high temperatures. This behavior may be interpreted as follows: at low temperatures, the L$\alpha$ emission is dominated by the scattering of incident radiation from the Sun, so that variations are weak; as a result of high opacity and albedo, most photons are scattered. Between 10 000 and 20 000 K, the collisional excitation process becomes more and more efficient and raises the population of level 2, and consequently the L$\alpha$ source function. At temperatures higher than 20 000 K, the source function continues to increase, but the optical thickness rapidly drops as a result of ionization, so that the intensity finally decreases. The other Lyman lines show similar behavior, but the maximum of intensity is located at a higher temperature. Balmer and Paschen lines also show small variations under a temperature of 10 000 K: there is a balance between the decrease in optical thickness and the increase in source function. At higher temperatures, the decrease in optical thickness dominates, and the lines vanish progressively.

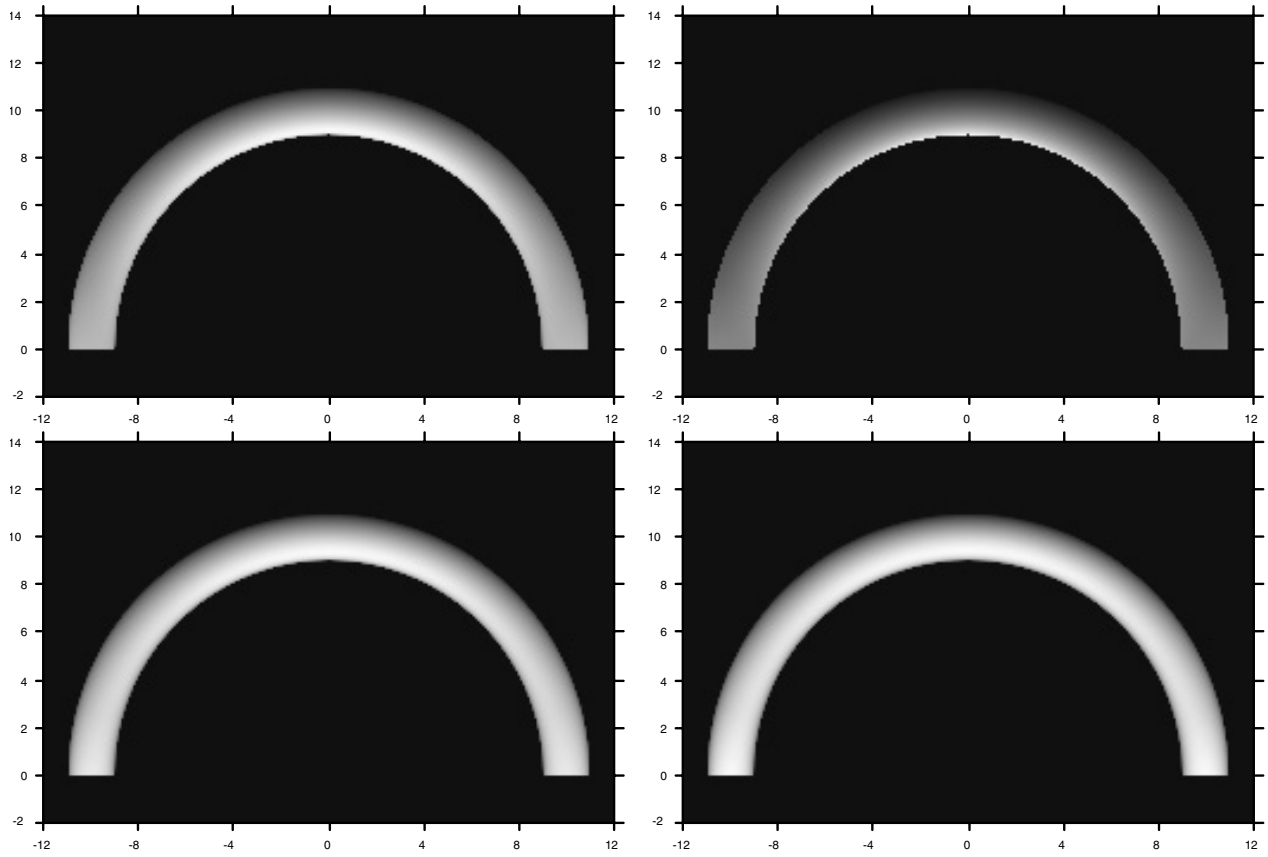

**Fig. 2.** Emission of the loop model 2 in different lines: L$\alpha$ (*top, left*), L$\beta$ (*top, right*), H$\alpha$ (*bottom, left*), H$\beta$ (*bottom, right*). Frequency–integrated intensities are normalized to the maximum value of each image, i.e. (in erg cm$^{-2}$ s$^{-1}$ sr$^{-1}$): $4.55 \times 10^4$ for L$\alpha$, $1.13 \times 10^2$ for L$\beta$, $5.94 \times 10^4$ for H$\alpha$, and $6.86 \times 10^3$ for H$\beta$.

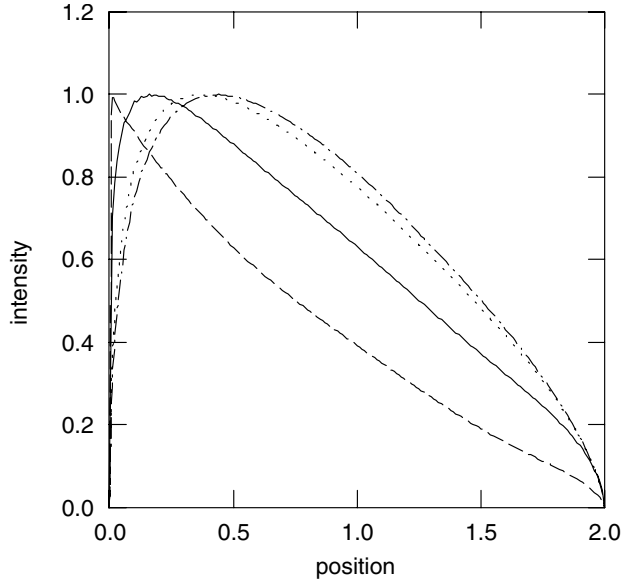


**Fig. 3.** Relative intensity variations across the top of the loop for Model 2 (intensities are integrated over frequency). Abscissae (in Mm) run from the internal side to the external one. Full line: L$\alpha$; dashed line: L$\beta$; dotted line: H$\alpha$; dot-dashed line: H$\beta$.

The transition between the optically thick and optically thin regimes when temperature increases is very clear in Fig. 6, which represents the relative variations in intensity across the top of the loop. At 5000 K, the maxima of intensity for the three lines (L$\alpha$, L$\beta$ and H$\alpha$) are located close to the lower edge of the loop, while at 30 000 K, they are approximately in the middle of the structure. This effect is due not only to the decrease in optical depths, but also to the change in the dominant emission mechanism: scattering at 5000 K, collisional excitation at 30 000 K.

### 3.4. Pressure effects

With the help of models 1, 2, and 3, it is possible to study the effects of gas pressure on the emitted intensities. For the relatively low temperature of 7500 K, scattering is the dominant process of emission. There is a striking difference of behavior between Lyman and Balmer lines, which is a result of the difference in opacities. As may be seen in Fig. 7, the profiles of intensity variations across the top of the loop are weakly affected in the case of L$\alpha$ and L$\beta$. In contrast, when the pressure varies from 0.02 to 0.5 dyn cm$^{-2}$, the H$\alpha$ line changes from the optically thin case to the optically thick one, and the maximum of intensity is displaced from the middle of the structure to the lower edge. A similar effect is observed concerning the absolute intensities: when the pressure is multiplied by 25, the maximum intensity in L$\beta$ varies by a factor of about 2 (from 94 to 166 erg cm$^{-2}$ s$^{-1}$ sr$^{-1}$). At the same time, the maximum H$\alpha$

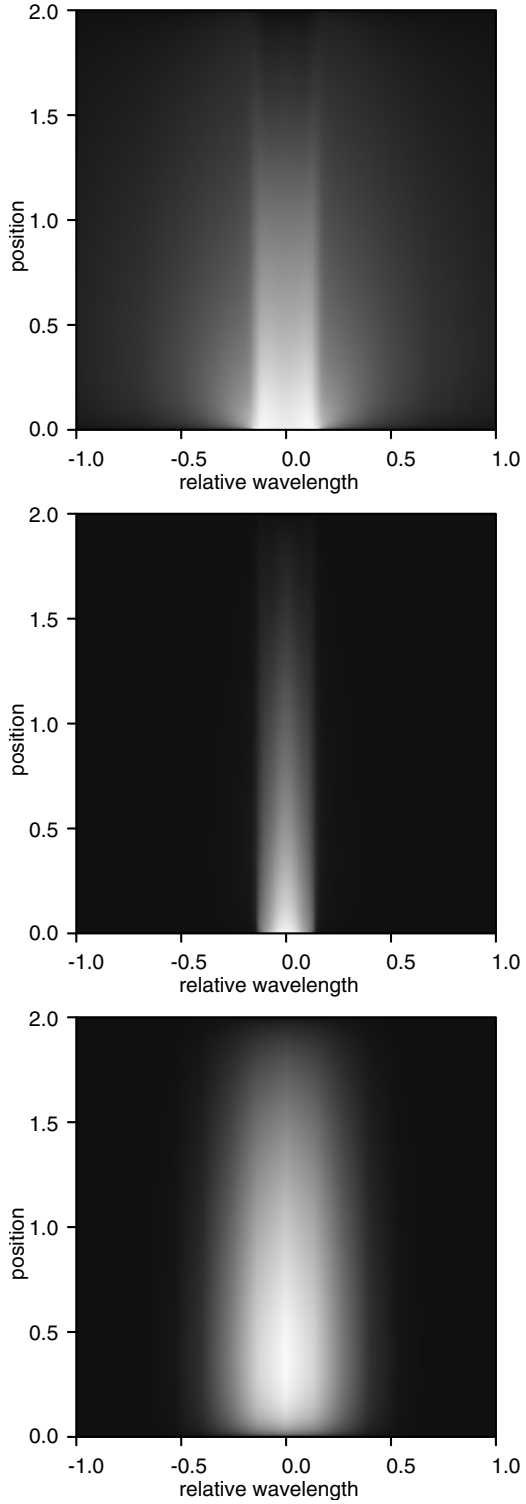


**Fig. 4.** Specific intensity variations across the top of the loop for Model 2 as a function of wavelength (in Å, relatively to line center) and position (same definition as in Fig. 3) for three hydrogen lines. Intensities are normalized. *Top*: L$\alpha$; *middle*: L$\beta$; *bottom*: H$\alpha$.

intensity is multiplied by more than 20 (from $8.7 \times 10^3$ to $2.1 \times 10^5$ erg cm$^{-2}$ s$^{-1}$ sr$^{-1}$).

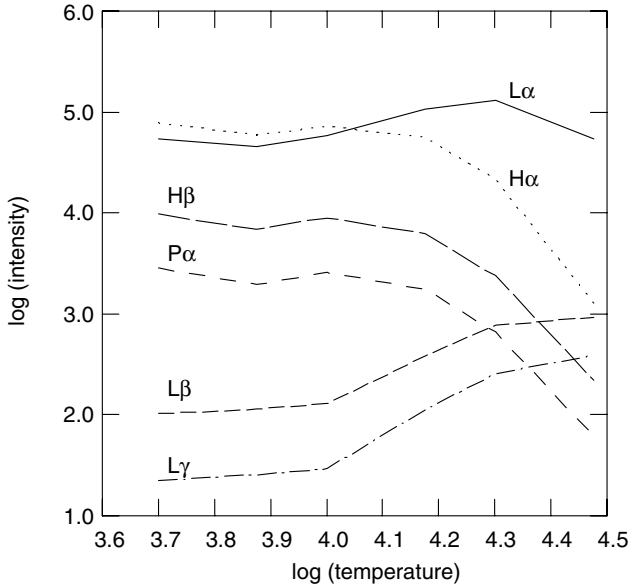


**Fig. 5.** Maximum frequency-integrated intensity as a function of temperature for six important lines of hydrogen (intensity unit: erg cm$^{-2}$ s$^{-1}$ sr$^{-1}$).

## 4. Loops with a radial temperature gradient

The objects under study are relatively cool and dense structures embedded in the hot and tenuous coronal medium. This is the case, in particular, for spicules and prominence threads. The isothermal models studied above assume that the transition between the two media is infinitely thin or, at least, that its effect on emitted intensities is negligible. This situation seems unlikely with respect to most observations, where the appearance of the structures varies with the temperature of spectral line formation. Instead, the size of observed structures seems to increase with the temperature of formation, which shows the importance of a proper treatment of transition regions when modelling these objects.

### *4.1. Model*

We do not try to construct a model here on theoretical grounds: our aim is simply to show the effect of a radial temperature gradient on the intensities of hydrogen lines and continua, with a model that contains as few arbitrary parameters as possible. So, the overall size of the preceding models is retained, with radii of 1 Mm for the torus section and 10 Mm for the axial circle. The gas pressure is kept to 0.1 dyn cm$^{-2}$. As to temperature, the loop contains an isothermal core at $T_0$, extending from $r = 0$ to $r = r_0$, and a transition zone from $r = r_0$ to $r = r_1$, where $T$ varies according to:

$$\log T(r) = \log T_0 + (\log T_1 - \log T_0)\frac{r - r_0}{r_1 - r_0}. \quad (1)$$

In the present case, the constants have the following values: $r_0 = 500$ km, $r_1 = 1000$ km, $T_0 = 6000$ K, and $T_1 = 10^5$ K. The transition region should extend to coronal temperatures of about $10^6$ K, but those regions hotter than $10^5$ K contain practically no neutral hydrogen, so that their contribution to absorption or emission in hydrogen transitions may be neglected.

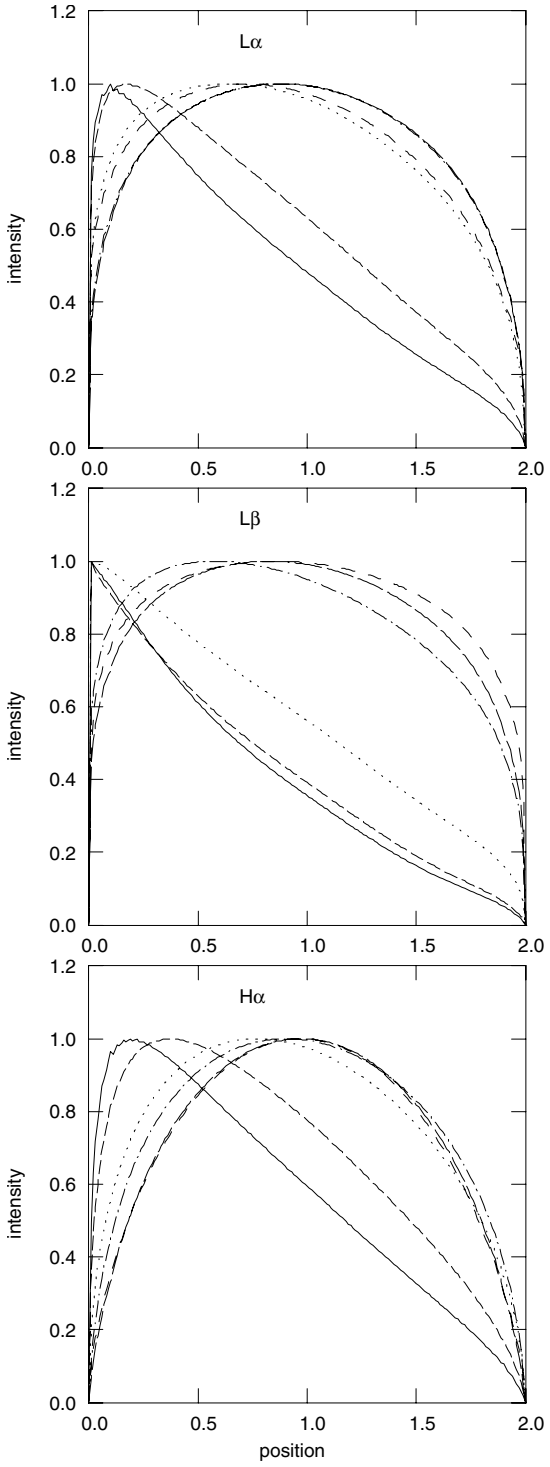


**Fig. 6.** Relative intensity variations across the top of the loop for different temperatures (intensities are integrated over frequency). Abscissae are the same as in Fig. 3, and pressures are equal to 0.1 dyn cm$^{-2}$. Temperatures: full line: 5000 K; dashed line: 7500 K; dotted line: 10 000 K; dash-dotted line: 15 000 K; long dashes: 20 000 K; spaced dashes: 30 000 K. *Top panel*: L$\alpha$; *middle*: L$\beta$; *bottom*: H$\alpha$.

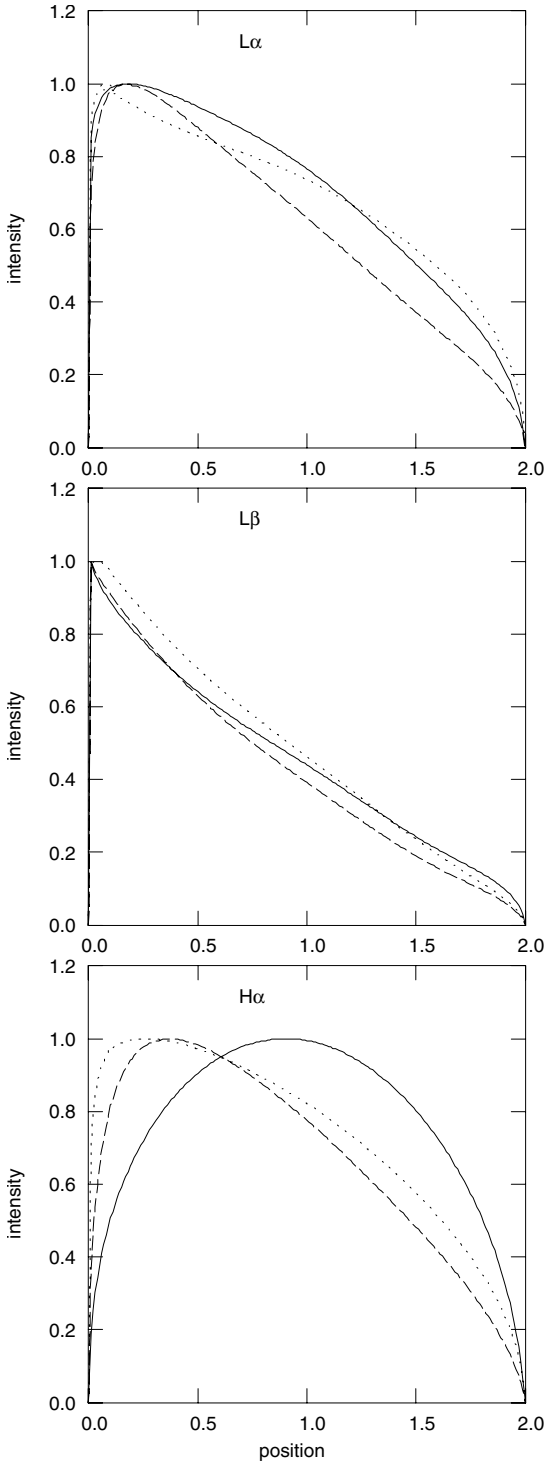


**Fig. 7.** Relative intensity variations across the top of the loop for different gas pressures. Abscissae are the same as in Figs. 3 and 6. Temperature: 7500 K. Pressures (in dyn cm$^{-2}$): full line: 0.02; dashed line: 0.1; dotted line: 0.5. *Top panel*: L$\alpha$; *middle*: L$\beta$; *bottom*: H$\alpha$.

### *4.2. Line intensities*

The appearance of the loop is shown in Fig. 8 for different transitions: L$\alpha$, L$\beta$, H$\alpha$, and the Lyman continuum. The other Balmer lines, as well as the Paschen lines, are not represented, but they look very similar to H$\alpha$. The asymmetry between the upper and lower edges of the loop is still visible, but is weaker than in the case of cool isothermal loops. The most striking effect is the difference in apparent width of the loop between the Lyman and Balmer lines. This effect can be seen in more detail

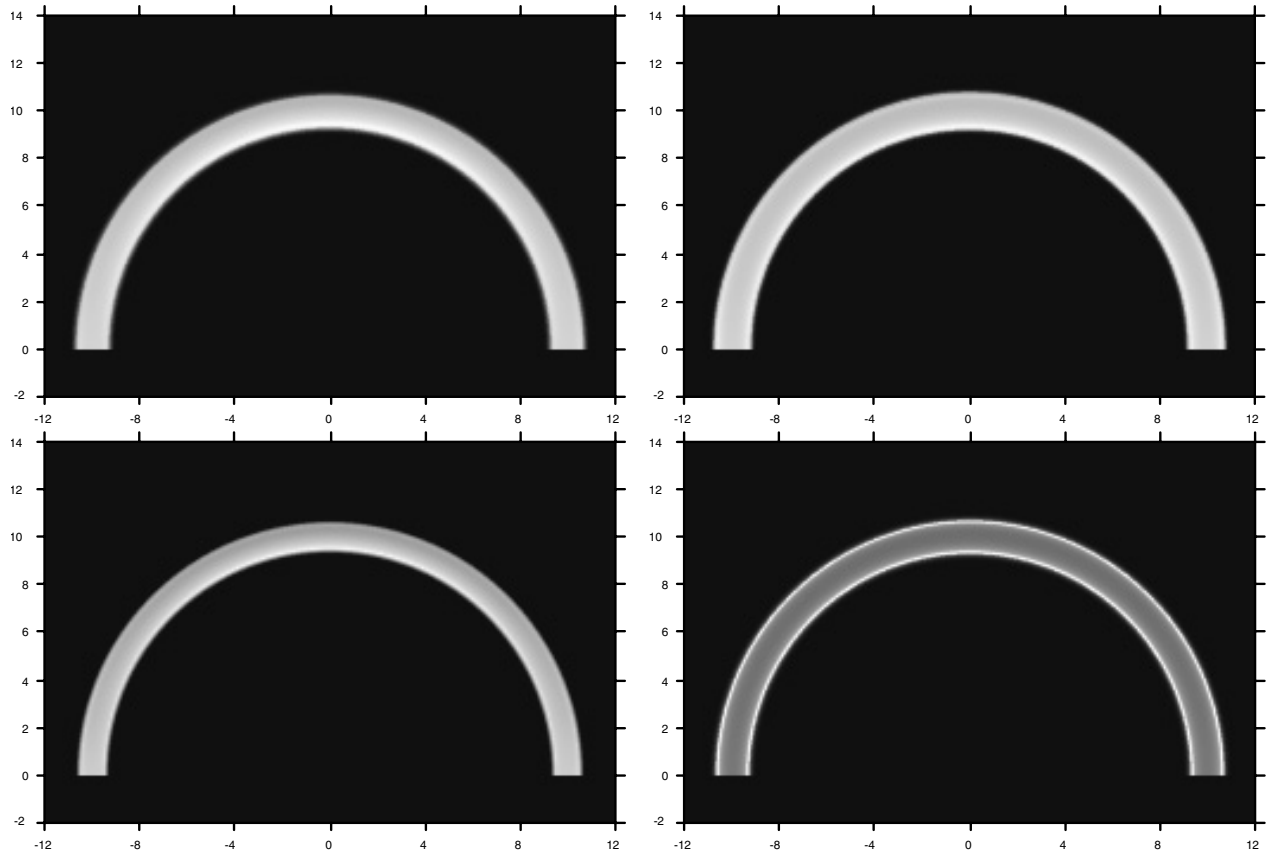

**Fig. 8.** Emission of the loop model with temperature gradient in several transitions: L$\alpha$ (*top, left*), L$\beta$ (*top, right*), H$\alpha$ (*bottom, left*), and Lyman continuum (*bottom, right*). Frequency-integrated intensities are normalized to the maximum value of each image: i.e. (in erg cm$^{-2}$ s$^{-1}$ sr$^{-1}$), $1.11 \times 10^5$ for L$\alpha$, $1.28 \times 10^3$ for L$\beta$, $7.90 \times 10^4$ for H$\alpha$, and $7.35 \times 10^3$ for the Lyman continuum.

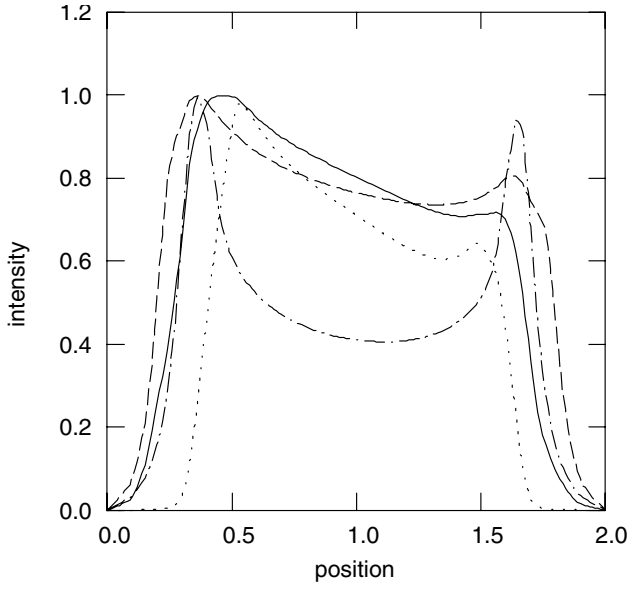


**Fig. 9.** Relative intensity variations across the top of the loop for the model with a radial temperature gradient. Abscissae (in Mm) run from the internal side to the external one. Full line: L$\alpha$; dashed line: L$\beta$; dotted line: H$\alpha$; dot-dashed line: Lyman continuum.

in Fig. 9, which represents the variations in intensity across the top of the loop. The part of the loop that is visible in H$\alpha$ is limited practically to the cool core of the structure, with a half width at half maximum of about 600 km, to compare with the core radius of 500 km. The same structure looks broader in Lyman lines, with an apparent radius of about 750 km, and is slightly broader in L$\beta$ than in L$\alpha$. The overall asymmetry is greater for L$\alpha$ than for L$\beta$, and for H$\alpha$ than for L$\alpha$.

### 4.3. Line profiles

These variations in intensity across the loop correspond to variations in the line profiles, which are displayed in Fig. 10. A comparison of this figure with Fig. 4 shows that the lines produced by the model with temperature gradient are broader than the corresponding lines emitted by the isothermal model at 7500 K. This is due to the contribution to emission of matter in the transition region, where the profile of the emission coefficient is thermally broadened. The L$\alpha$ line is strongly reversed on the main part of the structures, and it appears that it is the only reversed line for this model. Near the edges only, it becomes a pure emission line. In contrast, L$\beta$ and H$\alpha$ exhibit a nearly-Gaussian profile everywhere.

### 4.4. Lyman continuum

For this bound-free transition, the variation in intensity across the loop obtained with the temperature-gradient model is also

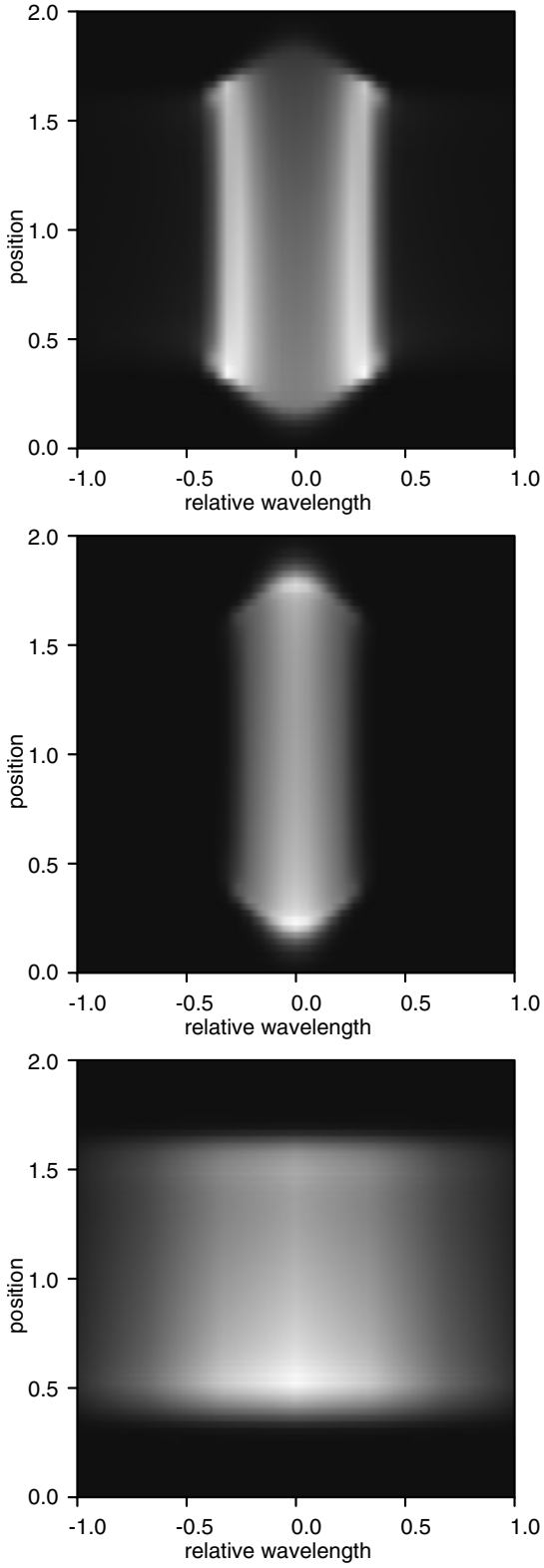


**Fig. 10.** Specific intensity variations across the top of the loop for the model with temperature gradient, as a function of wavelength (in Å, relatively to line center) and position (same definition as above), for three hydrogen lines. Intensities are normalized. *Top*: L$\alpha$; *middle*: L$\beta$; *bottom*: H$\alpha$.

very different from those obtained with the isothermal models. Figure 8 shows a reinforcement of emission near the edges of the loop, which is confirmed by Fig. 9: the spatial distribution of the Lyman continuum presents two peaks, whose intensity is about two times greater than its value in the middle of the structure. It appears that the main part of the Lyman continuum emission is formed in a layer of intermediate temperature (15 000−30 000 K) that is optically thin, while the core of the loop is dark and optically thick. The structure appears brighter close to the edge, where the length of the path through the emitting layer is at its maximum. This effect is similar to the limb-brightening observed for optically thin emission lines in the solar chromosphere.

## 5. Conclusion

A new computer code has been developed to treat the formation of hydrogen lines and continua in the filamentary structures of a stellar atmosphere. It is an NLTE radiative transfer code designed to solve the cylindrical 2D azimuth dependent problem. It allows the use of an arbitrary number of atomic levels for hydrogen. In the present case, we used 10 levels and 1 continuum for numerical applications. The electron density was computed simultaneously, in order to be consistent with hydrogen ionization. The present program can be used to predict the intensities and profiles of hydrogen lines emitted by thread-like structures embedded in the solar corona, whatever the inclination of their axes with respect to the solar surface. Two-dimensional distributions of pressure and temperature may be introduced into the computations, in order to study the emissive properties of rather complex theoretical models. The program might also be used for the modelling of observed structures, by means of an iterative process of comparison and correction.

Several developments are envisaged. The most useful for modelling is the extension to other atomic species that are currently being observed. Concerning hydrogen itself, the inclusion of partial frequency redistribution would be important to improve the treatment of Lyman lines, especially in cool structures (Heinzel et al. 1987). Finally, the method should be generalized to take into account the velocity fields associated with translation and rotation of matter inside the loops.

## References

Avery, L. W. 1970, Sol. Phys., 13, 301
Avery, L. W., & House, L. L. 1969, Sol. Phys., 10, 88
Avery, L. W., House, L. L., & Skumanich, A. 1969, JQSRT, 9, 519
Gouttebroze, P. 2004, A&A, 413, 733 (Paper I)
Gouttebroze, P. 2005, A&A, 434, 1165 (Paper II)
Gouttebroze, P., Vial, J.-C., & Tsiropoula, G. 1986, A&A, 154, 154
Heaslet, M. A., & Warming, R. F. 1966, JQSRT, 6, 751
Heasley, J. N. 1977, JQSRT, 18, 541
Heinzel, P., Gouttebroze, P., & Vial, J.-C. 1987, A&A, 183, 151
Leung, C. M. 1976, JQSRT, 16, 559
Magnan, C. 1970, JQSRT, 10, 1
Magnan, C. 1972, A&A, 21, 361
Ng, K. C. 1974, J. Chem. Phys., 61, 2680
Olson, G. L., Auer, L. H., & Buchler, J. R. 1986, JQSRT, 35, 431
Rybicki, G. B., & Hummer, D. G. 1991, A&A, 245, 171
Van Noort, M., Hubeny, I., & Lanz, T. 2002, ApJ, 568, 1066
Werner, K., & Husfeld, D. 1985, A&A, 148, 417